

# Dynamics of a Bio-Inspired Tail Modeled as an Elastic Beam Across Media, Loadings, and Material Properties

Marwan Fayed, Parsa Esfandiari

## Abstract

This project models a bio-inspired tail as a slender elastic beam actuated by a traveling curvature wave in low-Reynolds-number fluids. Using a planar discrete elastic rod formulation with analytic stretching and bending gradients/Hessians, we implement a fully implicit backward Euler integrator and a Newmark- $\beta$  scheme for verification. The model includes anisotropic viscous drag, heterogeneous bending stiffness, and spatially varying drag profiles. We validate baseline kinematics, compare integrator behavior, and run a 192-case sweep varying stiffness, geometry, density, viscosity, actuation amplitude, frequency, and fluid medium (water vs. glycerol). Metrics include net forward displacement, lateral excursions, and COM trajectories.

Results show that propulsion scales almost linearly with curvature amplitude and actuation frequency, while stiffness variations have only minor effects. A glycerol-like fluid yields displacements roughly three orders of magnitude larger than water, demonstrating the dominant role of viscous coupling. The framework provides a mechanics-based tool for analyzing how material and actuation choices influence propulsion in bio-inspired and soft robotic swimmers.

## 1. Introduction

Flexible tails and flagella are central to propulsion and maneuvering in a wide range of biological and robotic systems. Natural swimmers such as fish, eels, and spermatozoa generate thrust through traveling curvature waves along slender filaments, operating at Reynolds numbers where viscous drag dominates inertia and subtle changes in waveform strongly affect performance [1,4–7]. Classical studies of flagellar beating and anguilliform swimming quantified characteristic amplitude–frequency regimes and highlighted the nonlinear interplay between internal elasticity, active bending, and viscous loading [1,4,6,7].

Robotic implementations mirror these biological strategies: compliant tails and fins have been shown to enhance agility, energy efficiency, and robustness in both autonomous underwater vehicles and laboratory robotic fish [2,3,5,9,10].

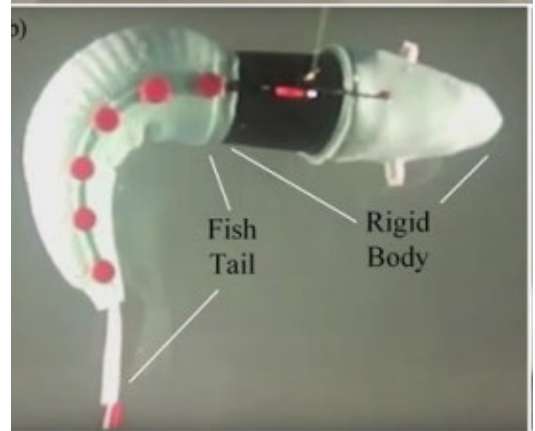


Figure 1. Classical Example of a robotic fish with an elastic tail [2]. Reviews of fish-like locomotion and robotic tails emphasize that carefully tuned flexibility and distributed actuation can improve maneuverability and disturbance rejection, but also stress the need for unified, mechanics-based simulation tools that can span different morphologies and fluid environments [2,6,10].

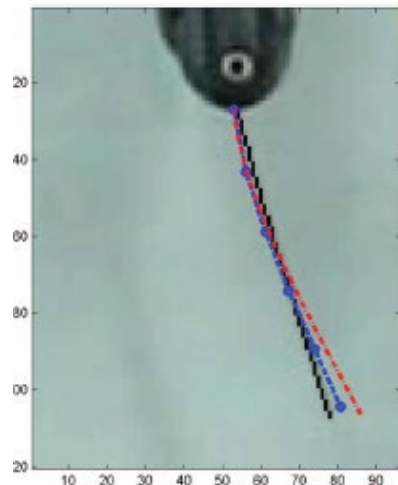


Figure 2. Comparison between experimental measurement of the time-dependent tail shape with model predictions [3].

Cosserat-rod and discrete elastic rod (DER) formulations provide an appealing foundation for such tools, as they capture stretching and bending in slender structures with high fidelity while remaining computationally tractable [1,8]. McMillen and Holmes used an elastic-rod model to study anguilliform swimming and its coupling to low-Reynolds hydrodynamics [1], while Bergou et al. developed the

DER framework that underpins many modern simulations of thin elastic filaments [8]. At the same time, hydrodynamic theories of microswimming and slender-body propulsion clarify how anisotropic drag and waveform kinematics set swimming speed and efficiency in viscous flows [6,7]. Base-actuated robotic fish with flexible tails, such as those modeled by Wang et al. and realized in soft-robotic platforms by Nguyen et al. and Katzschnmann et al., provide experimental benchmarks that directly connect rod-based structural models to measured trajectories and thrust generation [3,5,9].

Within this context, the present project develops a mechanics-grounded simulation framework for a curvature-driven, continuously deformable tail interacting with low-Reynolds viscous drag. By systematically varying stiffness distributions, actuation amplitude and frequency, material parameters, and fluid viscosity across different media, the framework aims to map out dynamic regimes and propulsive performance trends that are directly relevant to soft-robotic swimmers and biologically inspired tails [1–3,6,8–10].

## 2. Methods and Modeling Framework

### 2.1 Discrete Elastic Rod Model

The tail is modeled as a planar discrete elastic rod with  $N_v = 9$  nodes and  $N_e = N_v - 1 = 8$  edges. The generalized coordinate vector collects the nodal positions

$$\mathbf{q} = (x_0, y_0, x_1, y_1, \dots, x_{N_v-1}, y_{N_v-1})^\top \in \mathbb{R}^{2N_v}.$$

The rod has total length  $L = 1$  m and is initially straight along the  $x$ -axis, with uniform segment length

$$\Delta L = \frac{L}{N_v - 1}$$

We use an annular cross-section with outer radius  $R_{\text{outer}} = 0.013$  m, inner radius  $R_{\text{inner}} = 0.011$  m, elastic modulus  $Y = 70$  GPa(aluminum-like), and density  $\rho = 2700$  kg/m<sup>3</sup>.

From these we compute:

- Cross-sectional area

$$A = \pi(R_{\text{outer}}^2 - R_{\text{inner}}^2),$$

- Second moment of area (about z)

$$I = \frac{\pi}{4}(R_{\text{outer}}^4 - R_{\text{inner}}^4),$$

- Stretching stiffness  $EA = YA$ ,
- Bending stiffness  $EI = YI$ .

Mass is lumped at the nodes, with each node assigned  $m_{\text{node}} = \rho A \Delta L$ , leading to a diagonal mass matrix  $M = \text{diag}(m_0, \dots, m_{2N_v-1})$ .

### 2.2 Elastic Energies

#### 2.2.1 Stretching Energy

Each edge behaves as an axial spring with reference length  $\Delta L$ . For edge  $k$  connecting nodes  $(x_k, y_k)$  and  $(x_{k+1}, y_{k+1})$ , the current edge length is

$$\ell_k = \sqrt{(x_{k+1} - x_k)^2 + (y_{k+1} - y_k)^2}.$$

The stretching energy is

$$E_k^s = \frac{1}{2} EA \Delta L \left( \frac{\ell_k - \Delta L}{\Delta L} \right)^2.$$

We implement analytic expressions for the gradient  $\nabla E_k^s$  and Hessian  $\nabla^2 E_k^s$  with respect to the four coordinates  $(x_k, y_k, x_{k+1}, y_{k+1})$ . Global stretching forces and stiffness are assembled by looping over edges, resulting in the stretching force  $\mathbf{F}_s = -\nabla E_s$  and the stretching Jacobian  $J_s = -\nabla^2 E_s$ .

#### 2.2.2 Bending Energy with Natural Curvature

Bending is formulated on triplets of consecutive nodes  $(k-1, k, k+1)$ . Using standard DER notation:

- Edge vectors

$$\mathbf{e} = \mathbf{x}_k - \mathbf{x}_{k-1}, \mathbf{f} = \mathbf{x}_{k+1} - \mathbf{x}_k,$$

- Unit tangents

$$\mathbf{t}_e = \frac{\mathbf{e}}{\|\mathbf{e}\|}, \mathbf{t}_f = \frac{\mathbf{f}}{\|\mathbf{f}\|},$$

- Curvature binormal

$$k_b = \frac{2 t_e \times t_f}{1 + t_e \cdot t_f}.$$

In 2D, we take the scalar curvature at node  $k$  as  $\kappa_k = (k_b)_z$ . We prescribe a time- and space-dependent natural curvature  $\kappa_0(s_k, t)$  and define a local bending energy

$$E_k^b = \frac{1}{2} \frac{EI_{\text{eff}}(s_k)}{\ell_k^{\text{Vor}}} (\kappa_k - \kappa_0(s_k, t))^2$$

where  $\ell_k^{\text{Vor}} = \Delta L$  is the Voronoi length and  $EI_{\text{eff}}(s_k)$  is a spatially varying bending stiffness (Section 2.3).

Using standard DER expressions, we compute the curvature gradients and Hessians  $\nabla \kappa_k$  and  $\nabla^2 \kappa_k$ , from which we assemble the bending force  $F_b = -\nabla E_b$  and the bending Jacobian  $J_b = -\nabla^2 E_b$ .

### 2.3 Curvature-Driven Actuation and Heterogeneous Stiffness

Rather than base forcing, we actuate the tail by prescribing a traveling natural curvature wave along arclength  $s$ :

$$\kappa_0(s, t) = \kappa_{\text{amp}} (0.2 + 0.8\xi) \sin(\omega t - k_{\text{wave}} s),$$

Here,  $\kappa_{\text{amp}}$  is the curvature amplitude,  $\omega = 2\pi f_{\text{act}}$  is the actuation angular frequency,  $k_{\text{wave}} = \frac{2\pi}{L}$  is the spatial wavenumber, and  $\xi = \frac{s}{L} \in [0, 1]$  is the normalized arclength.

The envelope  $0.2 + 0.8\xi$  increases curvature toward the tail while moderating excessively sharp bending at the head.

To approximate anatomical stiffening near the head, we use a smoothly varying effective bending stiffness

$$EI_{\text{eff}}(s) = EI(1 + a(1 - \xi))$$

so that the head ( $\xi \approx 0$ ) is roughly twice as stiff as the tail ( $\xi \approx 1$ ).

### 2.4 Viscous Drag: Anisotropic Stokes-Like Model

At low Reynolds number, viscous drag dominates inertia, so each edge is modeled as a slender segment with anisotropic drag characterized by a tangential coefficient  $\xi_{\parallel}$  and a normal coefficient  $\xi_{\perp} = \alpha \xi_{\parallel}$ , where a typical drag ratio is  $\alpha \approx 5$ .

For each edge we compute the local tangent  $t = (t_x, t_y)$  and normal  $n = (-t_y, t_x)$  in global coordinates, and form the local  $2 \times 2$  resistance tensor

$$R = \xi_{\parallel} tt^T + \xi_{\perp} nn^T.$$

This is lumped equally to the two edge nodes and assembled into a global damping matrix  $C \in \mathbb{R}^{2N_v \times 2N_v}$ .

The drag coefficients depend on the dynamic viscosity  $\mu$  and an equivalent radius  $R_{\text{eq}}$  derived from the cross-sectional area:

$$R_{\text{eq}} = \sqrt{\frac{A}{\pi}}, \quad \xi_{\parallel} = 6\pi\mu R_{\text{eq}}, \quad \xi_{\perp} = \alpha \xi_{\parallel}$$

We further allow a drag profile along the tail (e.g. a bulkier head):

$$\xi_{\parallel}^{(k)} = w_k \xi_{\parallel}, \quad \xi_{\perp}^{(k)} = w_k \xi_{\perp}$$

where  $w_k$  is a node-based weight; for example,  $w_0 = 10$  and  $w_k = 1$  for the remaining nodes, so the head experiences substantially larger drag.

The resulting viscous force is

$$F_v = -Cv,$$

with  $v = \dot{q}$  the nodal velocity vector.

### 2.5 Time Integration

The semi-discrete equation of motion is

$$Ma - F_s(q) - F_b(q, t) - F_v(v) - W = 0,$$

where  $W$  is the body force (e.g., gravity, which we set to zero for neutrally buoyant swimming).

#### 2.5.1 Implicit Euler

Our primary integrator is a fully implicit backward Euler scheme. Given  $(q^n, v^n)$  at time  $t_n$  with step size  $\Delta t$ , we approximate:

$$v^{n+1} \approx \frac{q^{n+1} - q^n}{\Delta t}, \quad a^{n+1} \approx \frac{v^{n+1} - v^n}{\Delta t}.$$

The force balance at  $t_{n+1}$  is

$$Ma^{n+1} - F_s(q^{n+1}) - F_b(q^{n+1}, t_{n+1}) - F_v(v^{n+1}) - W = 0.$$

We define the residual:

$$f(q^{n+1}) = Ma^{n+1} - F_s - F_b - F_v - W,$$

and solve  $f = 0$  using Newton–Raphson. The Jacobian includes the inertial contribution  $\frac{\partial(Ma)}{\partial q^{n+1}} \sim \frac{M}{\Delta t^2}$ , the elastic terms  $-(J_s + J_b)$ , and the viscous term  $-\frac{C}{\Delta t}$ .

### 2.5.2 Newmark– $\beta$ Integrator

We also implement a standard Newmark– $\beta$  scheme, Predictors:

$$\begin{aligned} q_{\text{pred}} &= q^n + \Delta t v^n + \frac{\Delta t^2}{2} (1 - 2\beta) a^n, \\ v_{\text{pred}} &= v^n + \Delta t (1 - \gamma) a^n \end{aligned}$$

Unknown at  $t_{n+1}$ :  $q^{n+1}$ , with

$$a^{n+1} = \frac{q^{n+1} - q_{\text{pred}}}{\beta \Delta t^2}, \quad v^{n+1} = v_{\text{pred}} + \gamma \Delta t a^{n+1}$$

We again enforce  $Ma^{n+1} - F_s - F_b - F_v - W = 0$  via Newton iteration, but the Jacobian now includes the dependence of both  $v^{n+1}$  and  $a^{n+1}$  on  $q^{n+1}$ . The viscous Jacobian contains an extra factor  $\frac{\gamma}{\beta \Delta t}$ .

Newmark– $\beta$  provides a more classical structural dynamics formulation and serves as an independent check on the implicit Euler implementation.

## 3. Simulation Setup and Metrics

### 3.1 Baseline Curvature-Driven Tail

For baseline studies we use  $N_v = 9$ , a total length  $L = 1$  m, a time step  $\Delta t = 5 \times 10^{-3}$  s, and a total simulation time of approximately  $T \approx 20$  s. The actuation parameters are a curvature amplitude  $\kappa_{\text{amp}} = 0.6$  and an actuation frequency  $f_{\text{act}} = 2$  Hz. The fluid has a water-like viscosity  $\mu = 10^{-3}$  Pa.s, an anisotropic drag ratio  $\frac{\xi_\perp}{\xi_\parallel} = 5$ , and gravity is turned off to enforce neutral buoyancy.

No positional boundary conditions were imposed on the rod; all nodes remained free so that the resulting locomotion emerged solely from the prescribed curvature actuation and viscous drag.

During each run we record the nodal positions  $(x_i(t), y_i(t))$ , the center-of-mass position  $x_{\text{COM}}(t)$ , the vertical displacements of the mid and tip nodes, and the horizontal displacements of the head and mid nodes. From these data we generate tail snapshots at selected time instants, the center-of-mass trajectory in the x–y plane, and time traces of  $x_{\text{COM}}(t)$  together with nodal displacements.

### 3.2 Propulsive and Stability Metrics

For each run we summarize performance with net forward displacement:

$$\Delta x_{\text{net}} = x_{\text{COM}}(T) - x_{\text{COM}}(0)$$

And maximum lateral COM excursion:

$$y_{\text{max}} = \max |y_{\text{COM}}(t)|$$

The parameter-sweep code is also set up to compute time-averaged energies and viscous power, including the mean stretching energy  $\langle E_s \rangle$ , mean bending energy  $\langle E_b \rangle$ , mean kinetic energy  $\langle E_k \rangle$ , and mean viscous power  $\langle P_v \rangle$ .

For the current sweep, a post-processing issue resulted in zero values for these energy metrics. We therefore focus our quantitative analysis on kinematic outputs ( $\Delta x_{\text{net}}$ ,  $y_{\text{max}}$ , and COM trajectories) and treat energetic analysis as future work.

### 3.3 Multi-Parameter Sweep Configuration

For the final study we run a 192-case multi-parameter sweep using the implicit Euler integrator. Each simulation spans  $T = 0.5$  s with time step  $\Delta t = 1 \times 10^{-4}$  s, which is small enough to ensure good Newton convergence and accurate kinematics.

The varied parameters are:

- Material stiffness scaling  
 $E \rightarrow E_{\text{factor}}, E_{\text{factor}} \in \{0.7, 1.0\}$ ,
- Radius / geometry scaling  
 $R \rightarrow R_{\text{factor}}, R_{\text{factor}} = 0.95$  (in this sweep),

- Density scaling  
 $\rho \rightarrow \rho_{\text{factor}}, \rho_{\text{factor}} = 0.90,$
- Viscosity scaling  
 $\mu \rightarrow \mu_{\text{medium}} \times \mu_{\text{factor}},$
- Medium
  - water (low viscosity),
  - glycerol-like (high viscosity),
- Curvature amplitude  
 $\kappa_{\text{amp}} \in \{0.8, 1.2\},$
- Actuation frequency  
 $f \in \{1.0, 1.5, 2.0\} \text{ Hz.}$

For each case we record the net COM displacement  $\Delta x$ , the maximum lateral COM excursion  $|y|_{\max}$ , a sample COM trace  $x(t)$ , and the nominal energy metrics.

## 4. Results

### 4.1 Baseline Tail Kinematics and COM Motion

In the baseline anisotropic-drag simulation, the prescribed curvature wave produces a clean, fish-like tail motion. The amplitude envelope  $0.2+0.8\xi$  leads to moderate midbody oscillations and larger, but controlled, deflections at the tip, with a smooth wave propagating from head to tail and no numerical artifacts. The heterogeneous stiffness (stiffer head, softer tail) limits excessive bending near the leading end, reducing yaw and promoting a primarily forward trajectory.

The center-of-mass trajectory shows steady forward drift with only small lateral excursions, while the mid- and tip-node vertical displacements highlight the expected growth in oscillation amplitude toward the tail. Horizontal displacements of the head and midbody nodes confirm that net forward displacement accumulates over successive cycles.

Taken together, these results show that curvature actuation combined with anisotropic drag and head stiffening produces coherent propulsion with improved directional stability compared to the earlier isotropic,

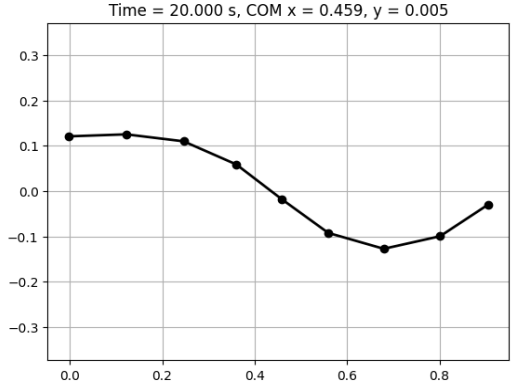


Figure 3. Tail configuration at  $t=20$  showing the deformed shape produced by the traveling curvature wave. The COM is located at  $x=0.459 \text{ m}, y=0.005 \text{ m}$

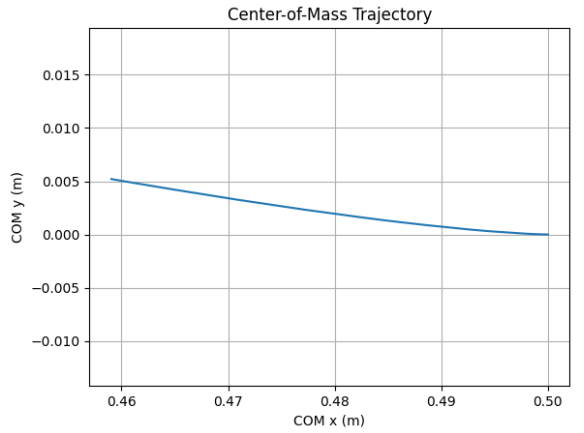


Figure 4. Center-of-mass trajectory in the  $x$ - $y$  plane, showing smooth forward drift with small lateral excursions.

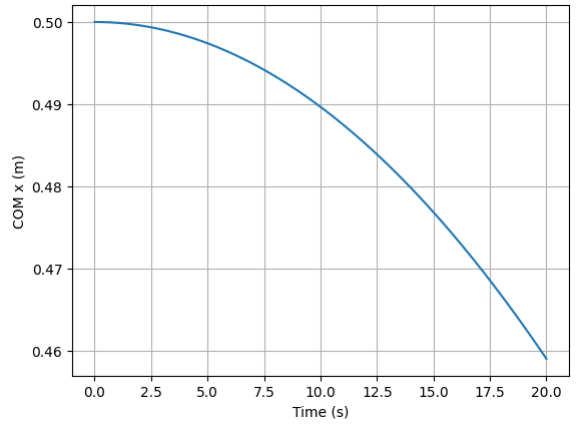


Figure 5. Horizontal COM position  $X_{\text{COM}}(t)$  over time, indicating steady net propulsion.

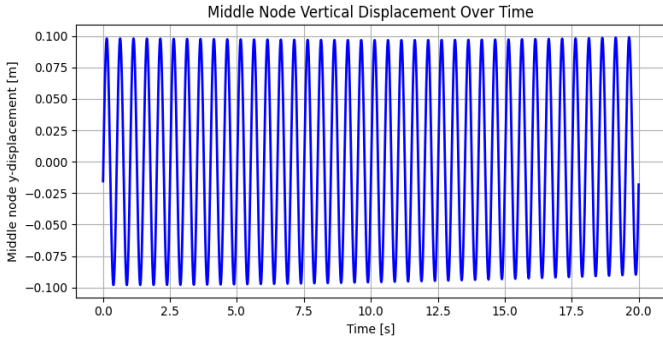


Figure 6. Vertical displacement of the midbody node, showing periodic oscillations with nearly constant amplitude

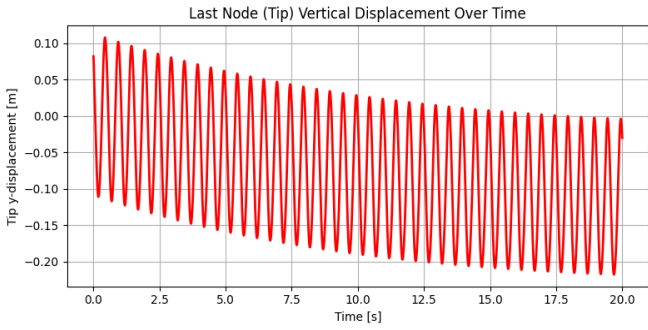


Figure 7. Vertical displacement of the tail tip, with larger oscillations and a slow downward drift due to the curvature envelope.

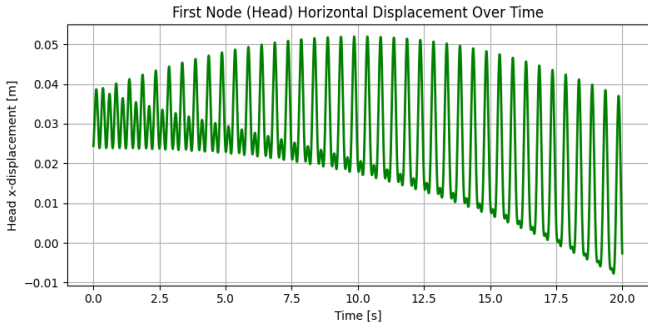


Figure 8. Horizontal displacement of the head node, showing small oscillations about a slowly drifting mean.

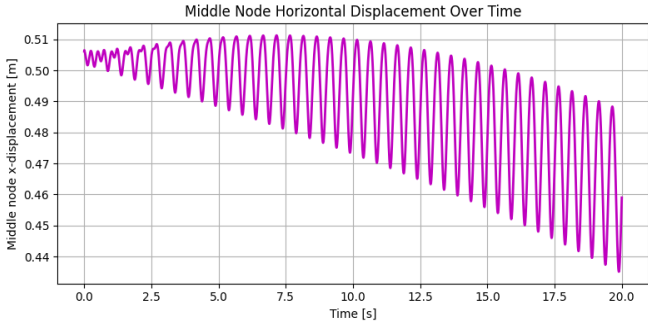


Figure 9. Horizontal displacement of the midbody node, combining oscillatory motion with gradual forward drift.

## 4.2 Implicit Euler vs Newmark- $\beta$

We compare the implicit Euler and Newmark- $\beta$  integrators in water for a moderate curvature amplitude ( $\kappa_{\text{amp}} = 0.5$ ) over  $T = 0.5$  s.

The Newmark scheme uses parameters  $\beta=0.5$  and  $\gamma=0.5$ . The COM  $x(t)$  trajectories produced by the two schemes nearly coincide, indicating that both methods remain stable for the chosen time step, that Newmark- $\beta$  introduces no noticeable phase lag or overshoot relative to implicit Euler, and that numerical dissipation is modest and comparable for both methods. This agreement justifies using the simpler implicit Euler method for the parameter sweep, with Newmark- $\beta$  retained as a cross-check.

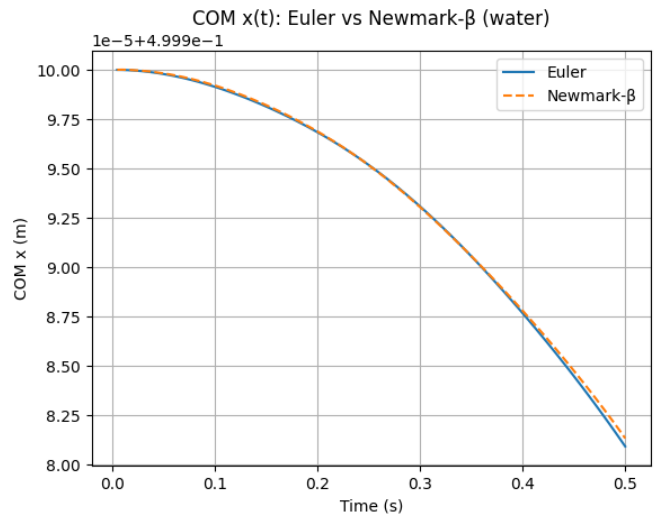


Figure 10. COM  $x(t)$  in water computed with implicit Euler and Newmark- $\beta$  ( $\beta=0.5$ ,  $\gamma=0.5$ ). The curves nearly overlap, confirming stability and close agreement between the integrators.

## 4.3 Multi-Parameter Sweep (Implicit Euler)

We now summarize trends observed in the full 192-case sweep, focusing on the kinematic observable  $\Delta x_{\text{net}}$ .

### 4.3.1 Effect of Stiffness Scaling $E_{\text{factor}}$

Figures “Net  $\Delta x$  vs  $E_{\text{factor}}$ ” in water and glycerol show that net displacement depends only weakly on stiffness over the tested range  $E_{\text{factor}} \in \{0.7, 1.0\}$ . In glycerol,  $\Delta x$  changes slightly as stiffness increases, but the curves for  $\kappa_{\text{amp}} = 0.8$  and 1.2 are almost flat. In water, the same trend appears at a much smaller magnitude (order  $10^{-5}$  m). This suggests that, as long as the rod is not so stiff that it cannot realize the prescribed curvature, nor

so soft that it collapses numerically, kinematics dominate over moderate stiffness variations for propulsion in this configuration.

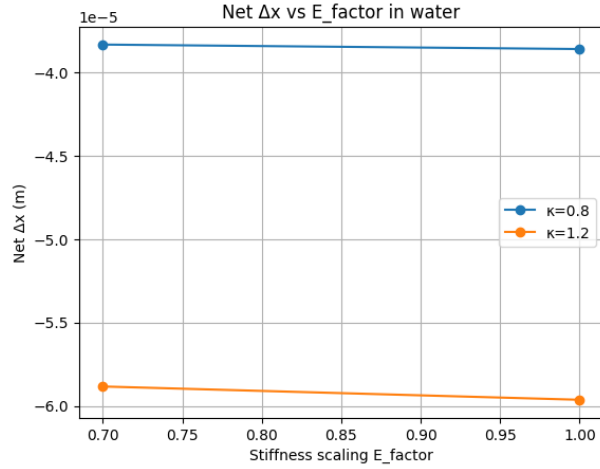


Figure 11. Net displacement  $\Delta x$  in water for stiffness scaling  $E_{\text{factor}} \in \{0.7, 1.0\}$  and curvature amplitudes  $\kappa_{\text{amp}} = 0.8$  and  $1.2$ . The curves are nearly flat, indicating weak sensitivity to stiffness.

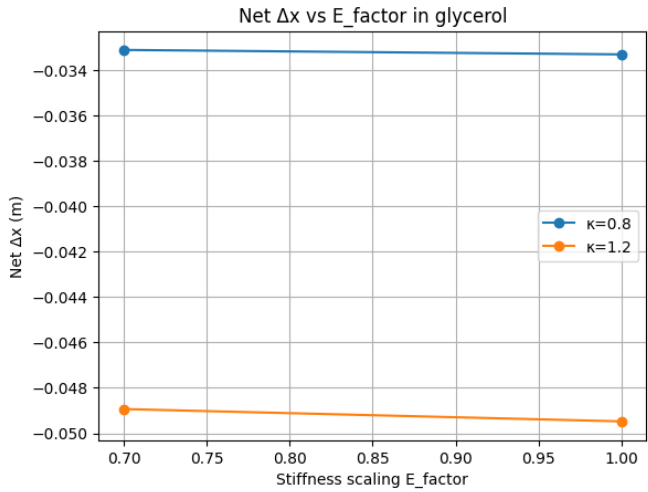


Figure 12. Net displacement  $\Delta x$  in glycerol for the same stiffness and curvature-amplitude values. A slight variation with stiffness is visible, but the dependence remains weak.

#### 4.3.2 Effect of Curvature Amplitude $\kappa_{\text{amp}}$

The “Net  $\Delta x$  vs  $\kappa_{\text{amp}}$ ” plots (for 0.8 and 1.2) show a strong, nearly linear relationship. For each frequency  $f = 1.0, 1.5, 2.0$  Hz, increasing  $\kappa_{\text{amp}}$  from 0.8 to 1.2 substantially increases  $|\Delta x|$ . In glycerol,  $|\Delta x|$  is on the order of  $10^{-2}$  m over 0.5 s interval and increases by roughly 50–60% between the low- and high-amplitude curves. In water, the absolute values of  $\Delta x$  are 3–4 orders

of magnitude smaller (order  $10^{-5}$  m), but the same monotonic trend with amplitude holds.

This is one of the clearest findings: stronger curvature waves produce stronger propulsion, consistent with elongated-body theory and experiments on flexible fins.

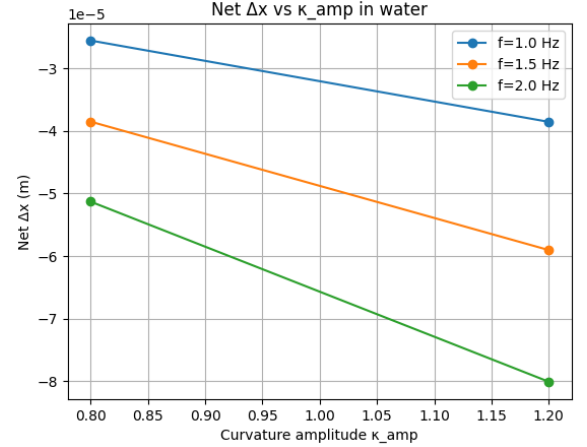


Figure 13. Net displacement  $\Delta x$  in water for curvature amplitudes  $\kappa_{\text{amp}} = 0.8$  and  $1.2$  at frequencies  $1.0$ – $2.0$  Hz. Displacements are small (order  $10^{-5}$  m) but increase nearly linearly with curvature amplitude and frequency.

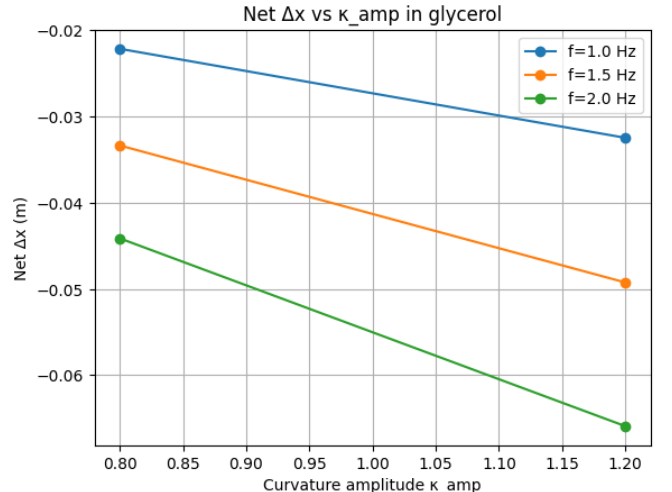


Figure 14. Net displacement  $\Delta x$  in glycerol for the same amplitudes and frequencies. Values are larger (order  $10^{-2}$  m) and show the same nearly linear dependence on curvature amplitude, with higher frequencies producing stronger propulsion.

#### 4.3.3 Effect of Actuation Frequency $f$

The “Net  $\Delta x$  vs frequency” plots for glycerol and water show that, for each stiffness factor,  $|\Delta x|$  increases almost linearly with frequency from  $f = 1.0$  to  $2.0$  Hz. In both media, the two stiffness curves (e.g.,  $E_{\text{factor}} = 0.7$  vs  $1.0$ ) nearly overlap, reinforcing that frequency and

curvature amplitude dominate propulsion compared to moderate stiffness changes. In glycerol, the slope of  $\Delta x(f)$  is large and negative—more cycles produce more net backward displacement in our coordinate setup. In water, the same trend appears but with much smaller magnitude.

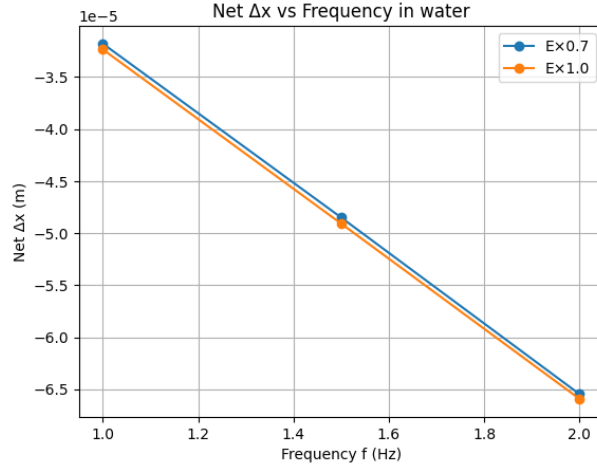


Figure 15. Net  $\Delta x$  versus actuation frequency in water. Displacement increases nearly linearly with frequency, and stiffness has minimal influence over the tested range.

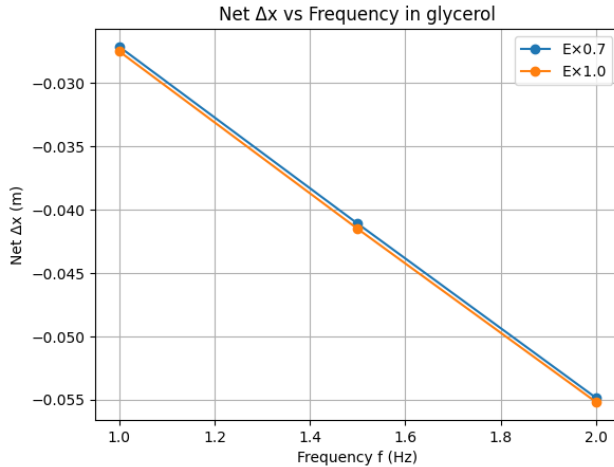


Figure 16. Net  $\Delta x$  versus actuation frequency in glycerol.

Displacement increases nearly linearly with frequency, and the two stiffness levels produce almost identical trends.

#### 4.3.4 Representative COM Trajectories

A sample plot of COM  $x(t)$  for several parameter combinations (all in water) further illustrates these trends. All trajectories start from a common initial COM position and exhibit smooth, monotonic drift. Higher actuation frequency and larger curvature amplitude produce faster displacement, giving larger  $| \Delta x |$  at  $t = 0.5$  s. No spurious oscillations or numerical instabilities

are observed, confirming the robustness of the implicit Euler integrator under the chosen time step.

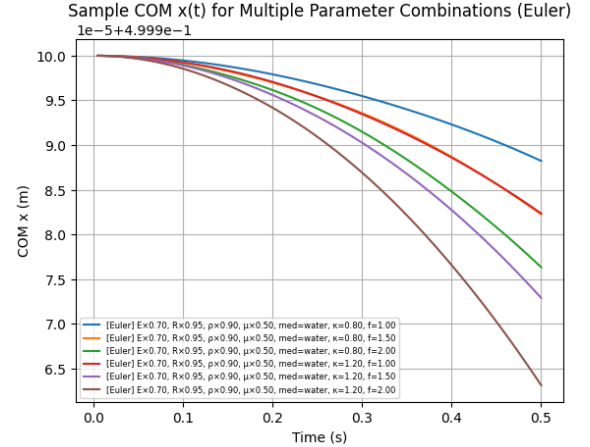


Figure 17. Sample COM  $x(t)$  trajectories in water for several combinations of curvature amplitude and frequency. Higher amplitudes and frequencies produce faster drift, and all curves remain smooth and stable under implicit Euler.

#### 4.3.5 Medium Comparison: Water vs Glycerol

Comparing the water and glycerol plots reveals a striking scale difference. In water, net displacements are on the order of  $10^{-5}$  m for the tested amplitudes and frequencies. In glycerol, net displacements increase to the order of  $10^{-2}$  m over the same 0.5 s interval. Thus, for this model and parameter set, a glycerol-like medium yields net displacements roughly three orders of magnitude larger than water. This reflects a combination of stronger drag forces for the same velocities, more effective conversion of lateral tail motion into net thrust, and the dominance of anisotropic drag over inertia in shaping the motion. All cases displace the COM in the same direction (negative  $\Delta x$ ), consistent with the propagation direction of the curvature wave.

## 5. Discussion

The final implementation provides a flexible platform for studying curvature-driven locomotion in slender tails, and several clear trends emerge from the simulations. First, within the tested range, moderate stiffness changes have only a small effect on net displacement, whereas curvature amplitude and actuation frequency show strong, nearly linear influence. This indicates that biological and robotic swimmers can tune performance primarily through their actuation patterns rather than through substantial structural

stiffness modifications, as long as the tail remains within a reasonable stiffness window.

Curvature amplitude and frequency function as effective design knobs: larger curvature waves and higher actuation frequencies consistently lead to stronger propulsion. In the modest frequency range explored (1–2 Hz), this growth is close to linear, reflecting the intuitive idea that more pronounced and more frequent bending transfers greater momentum to the surrounding fluid.

Viscosity also plays a central role in setting the propulsion scale. A glycerol-like medium produces net displacements roughly three orders of magnitude larger than water for the same actuation inputs. In this low-Reynolds-number regime, viscous forces dominate inertia, and greater drag effectively provides more “grip” for the tail to push against, enhancing thrust generation.

Across all 192 simulated cases, the direction of center-of-mass motion is consistently aligned with the direction of wave propagation. This robustness indicates that the curvature-driven mechanism remains stable under broad variations in stiffness, geometry, density, viscosity, and actuation parameters.

The comparison between implicit Euler and Newmark- $\beta$  (with  $\beta=0.5$ ,  $\gamma=0.5$ ) shows that both integrators produce nearly identical kinematic results under water-like conditions. This justifies using the simpler implicit Euler method for large parameter sweeps, while retaining Newmark- $\beta$  as an alternative for future studies involving more detailed transient or energetic analysis.

Finally, although the codebase includes routines for computing stretching, bending, kinetic, and viscous dissipation energies, these metrics were not correctly populated in the present sweep. Resolving this post-processing issue would enable energy-based performance assessments, including propulsive efficiency and cost of transport, offering a natural extension of the current study.

## 6. Conclusions and Future Work

We have developed and implemented a curvature-driven, mechanics-based simulation framework for a

bio-inspired tail modeled as a discrete elastic rod interacting with viscous media. The model integrates natural curvature actuation, anisotropic and spatially varying drag, and fully implicit time integration using both an implicit Euler scheme and a Newmark- $\beta$  formulation. A comprehensive multi-parameter sweep was performed across mechanical, geometric, and fluid variables to examine how these factors influence propulsion.

The results show that curvature amplitude and actuation frequency are the most effective levers for controlling net displacement, with both parameters producing strong, nearly linear changes in propulsion. Variations in stiffness over the tested range have only secondary influence by comparison. The simulations further reveal that a glycerol-like, high-viscosity medium produces net displacements roughly three orders of magnitude larger than water under the same actuation conditions, underscoring the dominant role of viscous coupling in low-Reynolds-number environments. The agreement between implicit Euler and Newmark- $\beta$  trajectories confirms that both integrators are stable and consistent for the parameter space explored.

This framework provides a foundation for future studies in bio-inspired locomotion and soft robotics. Natural extensions include incorporating more detailed hydrodynamic representations—such as Resistive Force Theory or slender-body theory—to better link tail kinematics to thrust and swimming speed; modeling transitions between media, such as air–water or water–gel interfaces; and extending the rod formulation to three dimensions to capture torsion and more realistic fin or tail dynamics. Completing the energy computation pipeline will also enable evaluations of propulsive efficiency and support inverse-design studies targeting optimal stiffness gradients, actuation profiles, and geometries for efficient locomotion.

Overall, the project demonstrates that combining discrete elastic rod mechanics, curvature-based actuation, anisotropic drag, and robust implicit integration creates a powerful and extensible tool for exploring the physics and design space of bio-inspired tails.

Overall, the project demonstrates how combining discrete elastic rods, curvature-based actuation, anisotropic drag, and robust implicit integration yields a powerful tool for exploring the physics and design space of bio-inspired tails.

## 7. References:

- [1] T. McMillen and P. Holmes, “An elastic rod model for anguilliform swimming,” *Journal of Mathematical Biology*, vol. 53, pp. 843–886, 2006.
- [2] W. Saab, W. S. Rone, and P. Ben-Tzvi, “Robotic tails: A state-of-the-art review,” *Robotica*, vol. 36, no. 9, pp. 1263–1277, 2018.
- [3] J. Wang, P. K. McKinley, and X. Tan, “Dynamic Modeling of Robotic Fish With a Base-Actuated Flexible Tail,” *ASME Journal of Dynamic Systems, Measurement, and Control*, vol. 137, no. 1, 011004, 2015.
- [4] R. Rikmenspoel, “The tail movement of bull spermatozoa,” *Biophysical Journal*, vol. 5, no. 4, pp. 365–392, 1965.
- [5] P. L. Nguyen, V. P. Do, and B. R. Lee, “Dynamic modeling and experiment of a fish robot with a flexible tail fin,” *Journal of Bionic Engineering*, vol. 10, pp. 39–45, 2013.
- [6] E. Lauga and T. R. Powers, “The hydrodynamics of swimming microorganisms,” *Reports on Progress in Physics*, vol. 72, 096601, 2009.
- [7] J. Lighthill, “Flagellar hydrodynamics,” *SIAM Review*, vol. 18, no. 2, pp. 161–230, 1976.
- [8] M. Bergou, B. Audoly, E. Vouga, M. Wardetzky, and E. Grinspan, “Discrete elastic rods,” *ACM Transactions on Graphics*, vol. 27, no. 3, pp. 1–12, 2008.
- [9] R. K. Katzschatmann, J. DelPreto, R. MacCurdy, and D. Rus, “Exploration of underwater life with an acoustically controlled soft robotic fish,” *Science Robotics*, vol. 3, no. 16, eaar3449, 2018.
- [10] M. Sfakiotakis, D. M. Lane, and J. B. C. Davies, “Review of fish swimming modes for aquatic locomotion,” *IEEE Journal of Oceanic Engineering*, vol. 24, no. 2, pp. 237–252, 1999.